Self-excited fluidic oscillators for cooling enhancement in gas turbines: an experimental and computational study

J. S. Ten[1] and T. Povey[2]
University of Oxford, Parks Road, Oxford, OX1 3PJ.

Pulsed flow has been shown to enhance heat transfer coefficients of impinging jets. This paper considers the use of pulsed impinging jets, derived from a self-excited fluidic oscillator, for gas turbine cooling. Self-excited oscillatory behavior was demonstrated in simulations over a wide range of inlet to outlet pressure ratios from p_{01}/p_2 = 1.0025 to p_{01}/p_2 = 2.18 for a device with a nozzle throat to splitter length of 10.4 mm. Heat transfer simulations at two test points (460 Hz and 769 Hz) resulted in Nu enhancement of 13% and 15% over corresponding cases with non-periodic flow at the same time mean mass flow rate. Increased oscillation frequency was found to increase Nu enhancement. In the range 10 kHz $< f <$ 20 kHz ($0.04 < fL/v < 0.08$) the Nu approximately doubled. A computational geometry optimization study was performed to increase oscillation frequency, resulting in a 30% increase. Validation experiments were performed using thin-film-gauge (high frequency) and calorimeter (low frequency) measurement techniques. Experimental results were broadly in line with numerical results, a Nu enhancement of approximately 20% (186 Hz $< f <$ 3 22Hz) was achieved. Despite the enhancement in heat transfer, the fluidic oscillator is far from an ideal solution due to extreme pressure losses inside the device.

Nomenclature

c_p = specific heat capacity

d = diameter

h = heat transfer coefficient

f = frequency

---

[1] Undergraduate Researcher, Department of Engineering Science; currently Doctoral Candidate, Department of Engineering, University of Cambridge.

[2] Professor of Engineering Science, Department of Engineering Science.

g = gas

i = inlet

L = characteristic length

k = thermal conductivity

m = mass

$\dot{m}$ = mass flow rate

p_0 = total pressure

p = static pressure

$\dot{q}$ = heat flux

$\dot{Q}$ = volumetric flow rate

t = time

T = temperature

v = average spatial velocity at nozzle outlet

V = voltage

w = wall

x = distance on impinging plate from the center of impinging jet

η = total pressure loss coefficient

τ = temperature decay time constant

I. Introduction

Impinging jets have been used since the 1960s as an effective way of enhancing heat transfer in cooling systems. The thin viscous and thermal boundary layers in the stagnation region of the impinging jet, and the high turbulence intensity of the jet lead to high local heat transfer coefficient. The effect of turbulence [1], [2] and nozzle type [3] have been investigated. There are a number of review articles which develop correlations for jet impingement heat transfer: for example [4], [5]. More recently the effect of pulsation on impinging jet heat transfer has been considered [6], [7], and has been shown in some cases to enhance heat transfer rates.

In tests of the cooling performance of a pulsing impinging water jet (square-wave pulsation) time-averaged Nusselt number enhancement of up to 33% over the constant mass flow-rate case was measured [8]. Time-averaged Nusselt number increases

up to 12% in the stagnation zone and 35% in the wall jet zone for intermittent pulsed impinging jets were achieved [9] in numerical simulations. In a recent numerical study of oscillating impinging jets a 100% improvement of heat transfer was reported [6] over conventional steady jets. The periodic disruption of and thinning of the boundary layer was the cause of the improvement.

Pulsating flow at moderately high frequency (up to approximately 1 kHz) can be achieved using mechanical methods. Investigators have used rotating cages to periodically open and close an orifice inside a cylinder to achieve sinusoidal alternating flow at frequencies of 1–750 Hz [10]. A rotating ball mechanism has also been used to generate a jet with pulsations at a frequency of 0–80 Hz and achieved heat transfer enhancement up to 12% near the nozzle mid-plane [11]. Mechanical valves are prone to wear of moving parts, however, and can be costly. They are also limited to relatively low frequencies.

Alternatively, acoustically shaped cooling holes that exploit the sequential pressure wave reflection mechanism have been use to improve cooling performance [12] by controlling the temporal discharge though an effusion cooling system in the presence of a high frequency (10 kHz) high amplitude external pressure wave caused by a passing rotor. This effect is highly significant, but there are relatively few natural applications of the concept. Sub-woofer speakers have also been used to excite an impinging jet at a nozzle and in a shear layer [13].

Periodic unsteadiness in the flow can also be self-induced by fluidic devices. A self-oscillating flapping flow has demonstrated heat transfer coefficient enhancements ranging from 20 % to 70 % in the range of 20-100 Hz [14]. Another periodic unsteady flow device that created a self-oscillating sweeping flow has shown improvements in the uniformity of heat transfer at the impingement plate [15]. This study considers self-excited fluidic devices as a means of providing pulsating flow for heat transfer enhancement at frequencies greater than 100 Hz. In section II of this paper, CFD simulations were used to develop the fluidic oscillator design. In section III, heat transfer simulations based on the output of the fluidic oscillator were performed to assess the enhancement in heat transfer due to the oscillating impinging jet. In section IV, the design of the fluidic oscillator was further optimized using results from the heat transfer simulations. The optimized fluidic oscillator was then manufactured and tested with findings reported in section V.

II.CFD development of fluidic oscillator

A design study of the fluidic oscillator was conducted using 2D CFD (ANSYS FLUENT 12.0), with further development in 3D CFD for comparison to experimental data. The initial design was made by combining a fluidic oscillator [16] with that of a fluidic valve [17]. The general geometry is shown in Fig. 1. A convergent nozzle feeds an oscillation chamber with

downstream splitter and two outlet tubes. Feedback tubes link the entrance to the oscillation chamber to exit of the oscillation chamber. The principle is that the flow through the nozzle first attaches to one side of the oscillation chamber, then feedback from the feedback tube detaches the flow, then the flow attaches to the other side. The process is continuously repeated. The nozzle throat is 0.5 mm in width, and the outlet tubes are 1 mm in width. The centerline throat to splitter distance is approximately 10.4 mm and the throat to outlet distance is 18.9 mm. The average cross-section length of feedback tube is 0.75 mm.

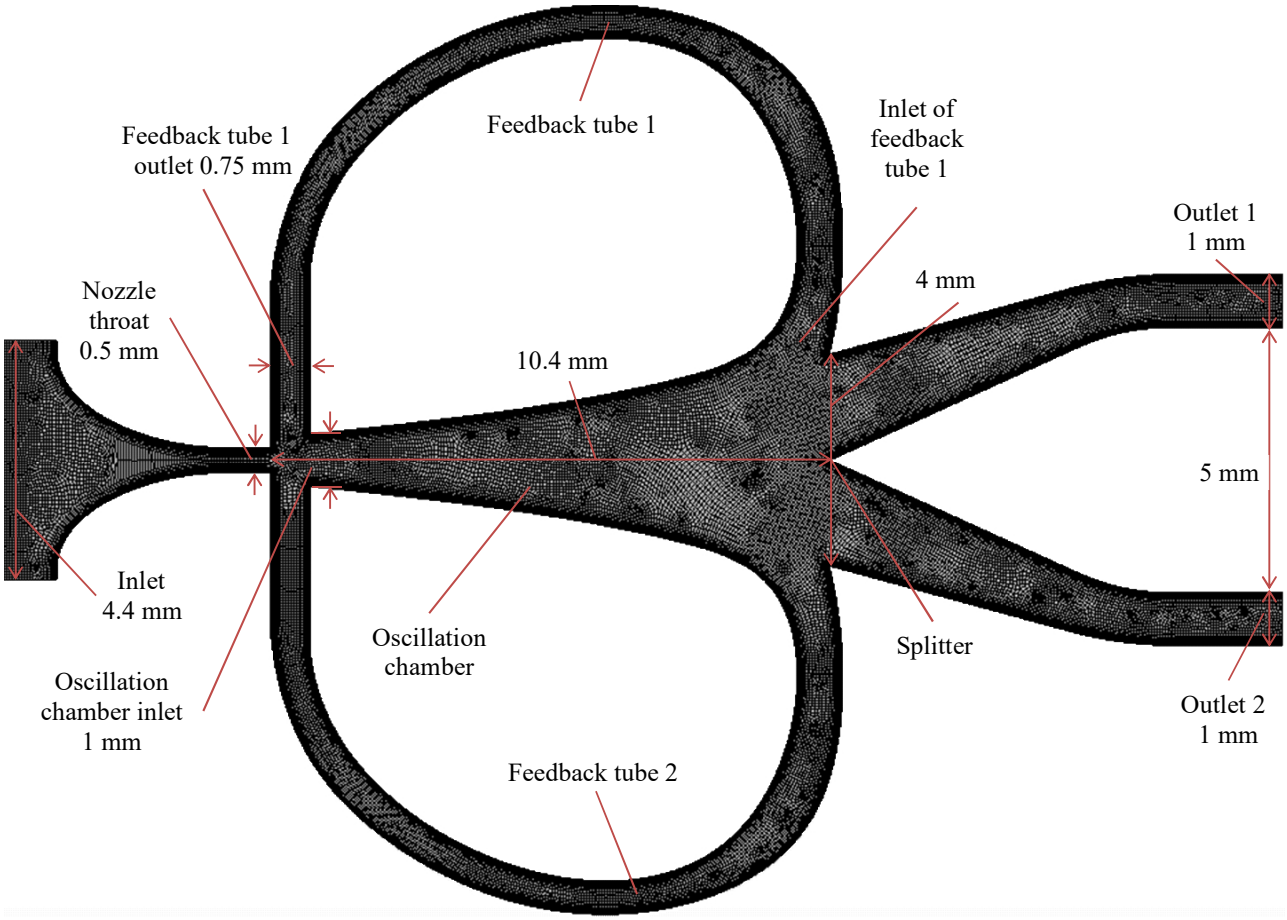

Fig. 1 Fluidic oscillator with nomenclature and dimensions of the parts.

The *k*-*ε* model [18] was used for turbulence modelling. The Aungier-Redlich-Kwong Real Gas model [19] was used to determine the density of air, and the Sutherland law [20] was used to determine the viscosity. The inlet was set as a pressure controlled inlet, the outlets as pressure outlets and all other walls as internal walls. Air was used as the fluid in the simulations. The turbulence intensity and viscosity ratio at the inlet was set to nominally low values, and are not thought to be influential because of the very strong acceleration at the inlet of the device, the extremely strong turbulence generation within the device

and the separated impinging jet at exit. Fine unstructured quadrilateral meshes (Fig. 1) were used for simplicity. 2D unsteady CFD simulations were conducted to investigate the relationships between the boundary conditions of the fluidic oscillator and the oscillation frequency, and to optimize the device geometry. The time step was set such that there were at least 30 steps per oscillation period, with 250 iterations per time step. Residuals were below 10^{-3}. Solutions were converged until the outlet mass flow rates were periodic, and then run for a further five oscillation periods.

A typical temporal outlet mass flow rate of the fluidic oscillator is shown in Fig. 2. Due to the symmetry of the design, the pulsed flow at the outlets are 180° out of phase to each other. At the minimum mass flow-rate, there is slight ingestion in the outlets.

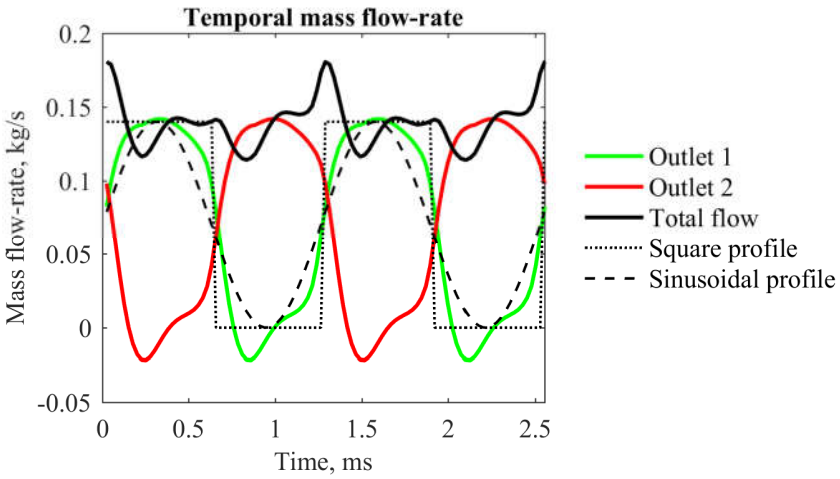

Fig. 2 Typical temporal outlet mass flow rate profile of the fluidic oscillator showing pulsed flow.

Operating characteristics for baseline design

Fig. 3 shows the results of simulations for 2D fluidic oscillators of the type shown in Fig. 1, for a variety of pressure ratios (in the range $1.0 < p_{01}/p_2 < 1.3$) and for four outlet pressures p_2 = 1, 4, 20, 40 bar. These pressures represent a Re (characteristic length based on outlet width of 1 mm and a velocity value spatially and temporally averaged over the outlet) range of 40. The effect of Re on f is greater at lower pressure ratios, resulting in an increase in f of up to 221% in the range $1.01 < p_{01}/p_2 < 1.10$ when the pressure outlet is at 1 bar. This is thought to be due to thinning of boundary layer regions in the oscillator.

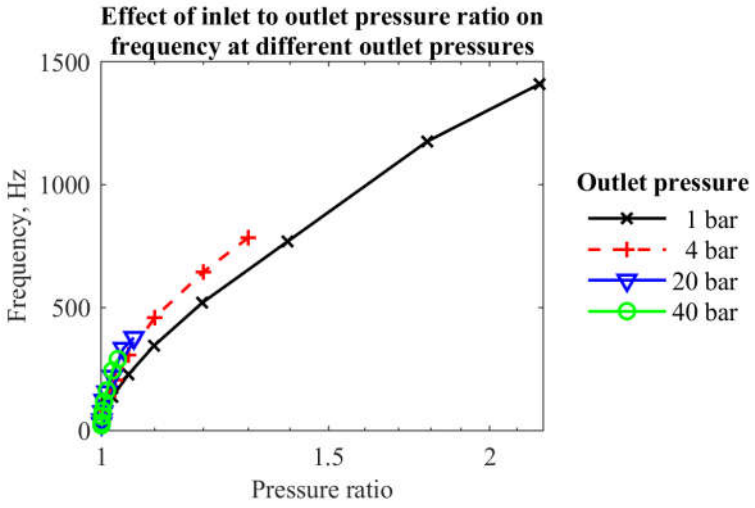

Fig. 3 Effect of pressure ratio on oscillation frequency.

A plot of f versus the time-mean Re, for the four outlet pressures p_2 =1, 4, 20, 40 bar is shown in Fig. 4. The direct proportional behavior of the frequency versus the Re agrees with experimental results on fluidic flow meters in [21].

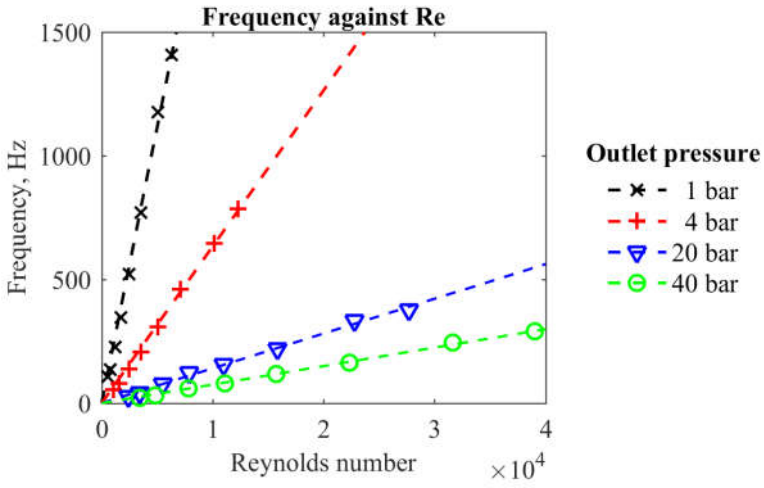

Fig. 4 Oscillation frequency as a function of Re.

Effect of physical scale

Table 1 shows the results of running the simulation at the original length scale ×1, ×2 and ×4. An inlet pressure of 4.4 bar and outlet pressure of 4 bar were used. This is a robustness check of the mass flow dependency, and the CFD solver. As expected, f roughly halves as the scale is doubled, whilst the volumetric flow-rate $\dot{Q}$, and therefore $\dot{m}$, approximately doubles. The parameter fL increases by 1.3% at ×2 scale, and increases by 7.8% at ×4 scale (here L is taken as the centerline nozzle

to splitter distance: 10.4 mm for the ×1 scale fluidic oscillator). This increase may possibly be attributed to the reduction in viscous surfaces per unit volume when the scale increases.

Table 1 Scaled fluidic oscillator simulation results.

Scale	p_{01}/p_2	f, Hz	fL, Hz.m	$\dot{m}$, kg/s	$\dot{Q}$, m^3 s^{-1}
1	1.1	460	4.784	0.279	0.0600
2	1.1	233	4.846	0.551	0.1185
4	1.1	124	5.158	1.090	0.2345

Effect of changing feedback tube aspect ratio

To understand the impact of the feedback tube length on the frequency response, a preliminary study with two tube lengths was investigated. Fig. 5 shows a short length tube (21.3 mm), and a long tube (41.9 mm).

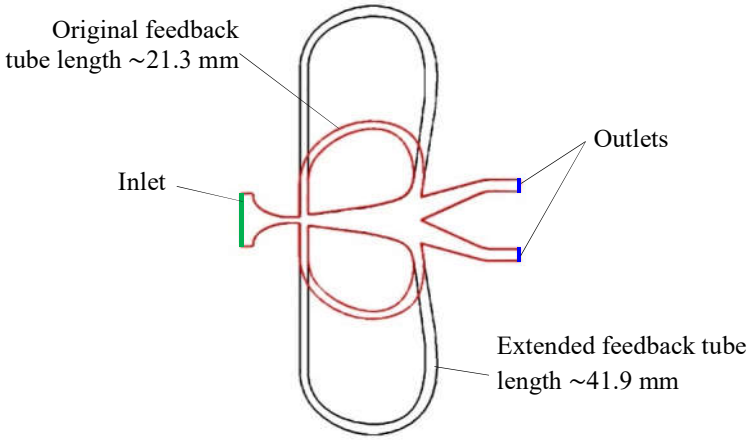

Fig. 5 Fluidic oscillator with original short feedback tube (red) and long tube (black).

Table 2 shows simulation results for a variety of inlet and outlet pressures for a short tube (1) and a long tube (2). The CFD predicted frequencies are f_1 and f_2 respectively. When the tube length was approximately doubled, the frequency change represented by f_1/f_2 was in the range $1.13 < f_1/f_2 < 1.34$. The frequency change appears to depend on both pressure ratio and Re (characteristic length based on one outlet width 1 mm and velocity spatially and temporally averaged over one outlet) and based on limited data does not show a clear trend (see, for example, the relatively complex behavior in Fig. 3). It is clear that the primary driver for the feedback mechanism is *not* a pressure wave propagating through the feedback tube – the tube is required to fill with flow to initiate the switching mechanism. To illustrate this point, the expected frequency, $f_2{}^*$, based on

acoustic wave propagation alone, is also presented in Table 2. Here f_2^* is calculated by modifying the CFD predicted value of f_1 to account for a pressure wave propagation time along a tube of length 20.6 mm (difference between long and short tubes). The speed of sound is taken to be 350 m/s (based on fluid properties at 300 K). Although the frequency shift is in the correct direction, the frequency modification f_1/f_2^* is only approximately 1.02 due to this mechanism. Thus, whilst a contributor, it is not the prime driver, which is ingestion of mass flow along the bypass loop.

Table 2 Simulation results for two tube lengths.

p_{01}, bar	p_2, bar	$\dot{m}$, kg/s	Re	f_1 CFD, Hz	f_2^*, Hz	f_2 CFD, Hz	f_1/f_2 CFD
1.02	1.01	0.0213	541	107.5	106.8	88.9	1.21
1.11	1.01	0.0683	1735	344.8	337.9	270.3	1.28
1.41	1.01	0.1378	3500	769.2	735.7	645.2	1.19
4.01	4	0.0426	1082	54.8	54.6	40.8	1.34
4.1	4	0.1384	3515	205.1	202.7	178.6	1.15
4.4	4	0.2792	7092	459.8	447.6	408.2	1.13

Extension to three-dimensional domain

The two-dimensional design was extruded by 1 mm to create a three- dimensional design, to assess the impact of additional wall losses on the fluidic behavior. Over the range tested (typical of the results presented above), good agreement between frequencies was observed between 2d and 3d designs, with mass flow rates the extruded 3d design typically a few percent lower than the 2d design (per mm of passage width). This reduction can be attributed to additional viscous surfaces.

III. Heat transfer simulations

In this section we consider the heat transfer enhancement due to impinging jets on a target surface. The Prandtl number of the air used in this study is 0.7. Thus, for accurate heat transfer simulations, the mesh quality must be higher than for accurate global flow pattern predictions. This is because the thermal boundary layer on the target surface is thinner than the viscous boundary layer. The dimensionless wall distance of the first node in the flow y^+ was kept under the value of 2 for the impinging jet wall.

Mesh independence study and CFD methods validation

The mesh independency and simulation validation study was done using a 2D axisymmetric computational domain (Fig. 6). For comparison, experimental results were taken from [22] which compiled results from [23] and [24]. In all of the experiments, the Re number was evaluated using a value of v spatially averaged at the nozzle inlet, and where the characteristic length L was the nozzle diameter d. For the experiments, the Re was 23,000 (except from [25] where the data was interpolated from cases at Re = 20,000 and 30,000) and the target-to-plate distance was $6d$.

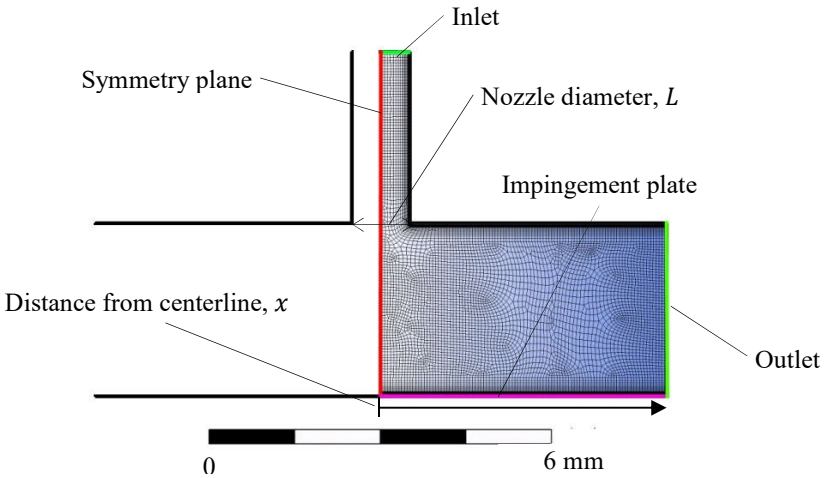

Fig. 6 2D axisymmetric mesh used in heat transfer simulations.

The simulations were run using three different mesh settings summarized in Table 3. The first column shows the mesh cell count, the second indicates the maximum size of an element far from the wall area (the *body* area), and the third shows the first layer thickness at the impingement plate. A growth factor of 1.2 was used between the wall mesh element and the body elements to provide a smooth transition between the different element sizes. Three different turbulence models were tested namely the *k-ε* model [18], the *k-ω* SST model [26] and the Spalart-Allmaras model [27].

Table 3 The different mesh settings that were used.

Mesh cell count	Body sizing, m	First inflation layer thickness, m
46×10^3	3.20×10^{-4}	1.00×10^{-6}
86×10^3	2.02×10^{-4}	6.30×10^{-6}
125×10^3	1.60×10^{-4}	5.00×10^{-6}

In Fig. 7, CFD simulation results are compared to the published experimental data mentioned previously. The *k-ε* model over-predicts the heat transfer rate significantly, whilst the Spalart-Allmaras model slightly under-predicts the heat transfer rate. The

k-ω SST model provides the best fit for the experimental data of heat transfer in impinging jets and this is in line with recommendations in [28]. The results of the simulation with 86×10^3 cells are similar to that with 125×10^3 cells, so the smaller cell count was used for the remainder of the heat transfer simulations.

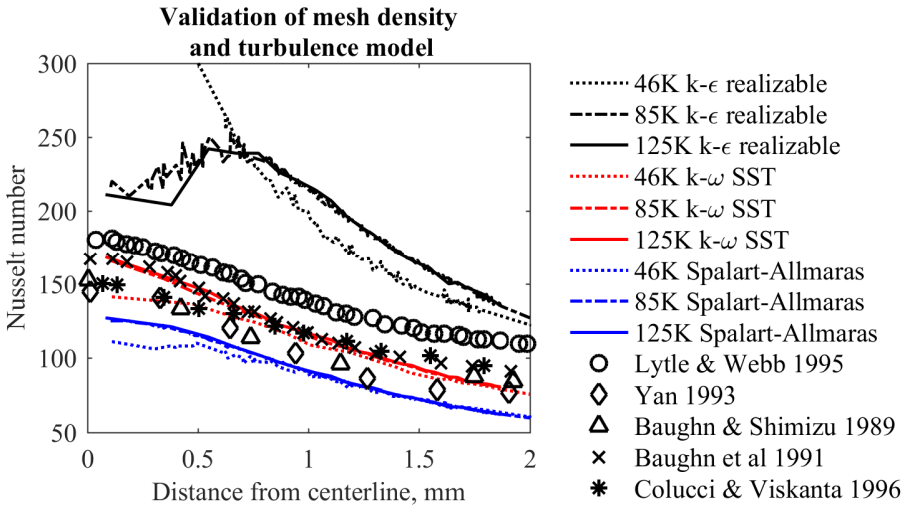

Fig. 7 Comparison of CFD results and published experimental data adapted from [22]**.**

Predicted heat transfer enhancement due to oscillatory behavior

The pulsing flow from one of the two outlets of the fluidic oscillator (Fig. 2) were recorded and used as the inlet mass flow rates for the heat transfer simulation. Two operating points were considered as seen in Table 4. For each setting a control with a constant mass flow rate equal to the average mass flow rate of the pulsed flow was also simulated.

Table 4 Settings for heat transfer simulation.

Setting no.	p_2, bar	p_{01}/p_2	$\dot{m}$, kg/s	Re	f, Hz
1	1.01	1.4	0.0695	3530	769
2	4.00	1.1	0.139	7074	460

The resulting Nu distributions for the oscillating impinging jet and the constant flow impinging jet are shown in Fig. 8. Here

$$Nu = hL/k \tag{1}$$

is based on h is the heat transfer coefficient (calculated by Fluent), L is the characteristic length (taken to be the nozzle width = 1 mm), and k is the conductivity of the fluid used which is air. Nu is presented as a function of distance from the jet center, presented in normalized form x/L. Time averaged values were used for the oscillating jet.

An enhancement in Nu is observed for the pulsed jet cases, which increases with distance from the stagnation point. The area average Nu (averaged over a surface length $0 < x/L < 5$) on the impingement plate was 15.5% higher for setting 1 and 13% higher for setting 2. The ratio of the peak Nusselt number which was achieved around the stagnation point is 1.5 times higher for setting no. 1 compared to setting no. 2. This agrees well with the prediction of 1.414 based on the standard flat plate correlations for forced convection laminar flow

$$Nu = 0.664 Re^{1/2} Pr^{1/3} \tag{2}$$

(see, for example, [29]). For forced convection turbulent flow, the prediction would be 1.741 based on the corresponding equation

$$Nu = 0.0296 Re^{4/5} Pr^{1/3} \tag{3}$$

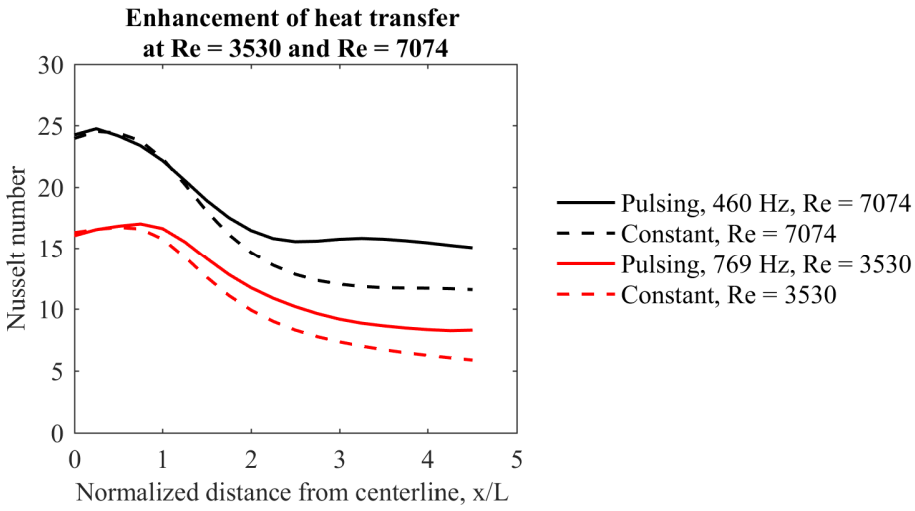

Fig. 8 CFD predictions of Nu distributions under an impinging jet, for both steady and oscillating jets.

Effect of oscillation frequency on Nu

To further investigate the relationship between heat transfer enhancement and oscillation frequency, simulations were conducted with both sinusoidal varying mass flow rates, square wave mass flow rates, and the pulsing flow profile of the fluidic

oscillator presented in Fig. 2. The pulsing frequency of one outlet of the fluidic oscillator as seen in Fig. 2 was artificially changed by scaling the oscillation time period to achieve a range of $10^2 < f < 10^6$. For all simulations the following conditions were used: p_2 =1.01 bar, $p_{01}/p_2 = 1.4$ and $\dot{m} = 0.0695$ kg/s (Re = 3530).

For each of the simulations, the area weighted average heat transfer coefficient was time averaged to produce a single area weighted and time averaged Nu value. Results are presented in Fig. 9, in which Nu is plotted as a function of frequency. The dominant feature is an increase in Nu enhancement up to $f = 10^4$ Hz, then a fairly steep trough, with a second increase in the enhancement for $f > 10^5$ Hz.

In general, there is reasonable agreement between the three pulsing profiles (square, sinusoidal, and fluidic oscillator profile) with peak enhancement in Nu of 2.25 times the baseline constant mass flow-rate Nu value at $f = 1 \times 10^4$ Hz. The square wave profiles produces slightly increased heat transfer enhancement compared to the sinusoidal wave profiles, in accord with the results of [7].

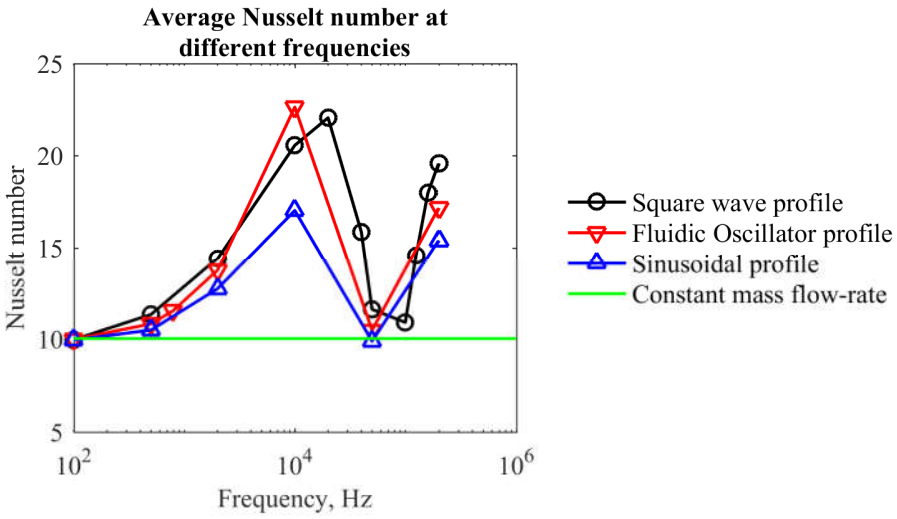

Fig. 9 Heat transfer simulation results at different impinging jet oscillation frequencies.

To assess the impact of Re, the square wave heat transfer simulations were repeated with the following conditions: p_2 = 4.00 bar, $\dot{m}$ = 0.139 kg/s (Re = 7074). The frequency was again artificially changed between simulations in the range $10^2 < f < 10^6$ Hz. To compare these predictions to those in Fig. 9, the dimensionless frequency (in parallel with the Strouhal number) *fL/v* was used. Here f is the frequency, L is taken as the width of the nozzle (1 mm) and v is the spatially and temporally averaged impinging jet velocity.

The results (Fig. 10) show that the general trends are similar, with greater heat transfer enhancement for the average Re = 7074 pulsing cases compared with the average Re = 3530 pulsing cases. Based on correlations for laminar flat plate heat transfer (given previously), we expect an enhancement of 1.414. A scaled trend line for Re = 3530 (scaled by 1.414) is presented. There is excellent agreement between the Re = 7074 results, and the correlation-scaled Re = 3530 results in the range $fL/v < 0.02$. Above this value the correlation-scaled Re = 3530 results are lower than the CFD predictions for Re = 7074. The peak in heat transfer enhancement is at fL/v = 0.08 for both Re = 3530 (corresponding to 20 kHz) and Re = 7074 (corresponding to 10 kHz).

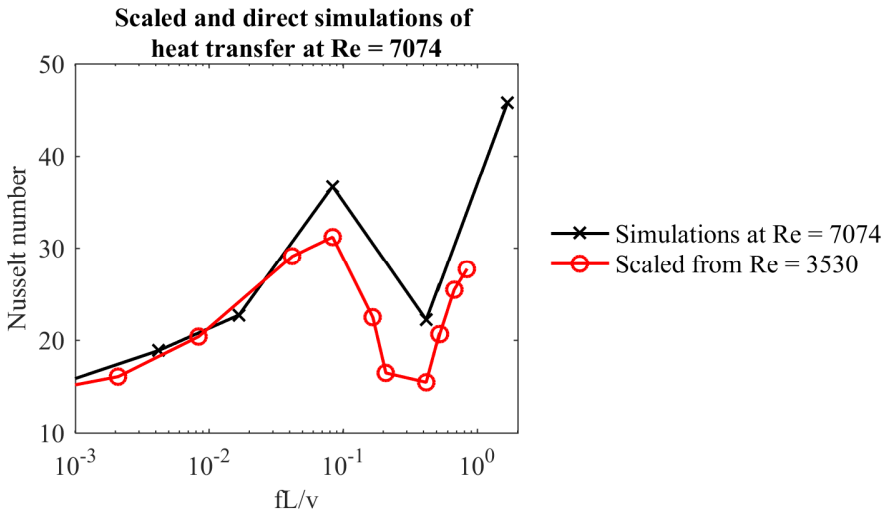

Fig. 10 CFD predicted Nu enhancement at Re = 7074 compared with correlation-scaled results at Re = 3530.

The peak Nu enhancement was likely due to vortex formation. For fL/v values close to the peak Nu enhancement (around fL/v = 0.08), the flow pattern for the Re = 7074 is shown in Fig. 11. High magnitude velocity jets (marked red in the figures) are seen to excite a vortex, which is convected across the gap (see progression of circles in figures (b) to (e)) and impinges on the surface. This vortex enhances the high velocity flow on the jet-impinged surface increasing the heat transfer rate. Similar plots away from the maximum in Nu enhancement show either weaker vortex formation (lower fL/v) or no vortex formation (higher fL/v), suggesting this mechanism may be significant. For normal impingement jets, the dominant frequency of the vortex structure is at fL/v=0.4 [30], this suggests that the oscillating impingement jet caused a significant reduction in the dominant frequency of the vortex.

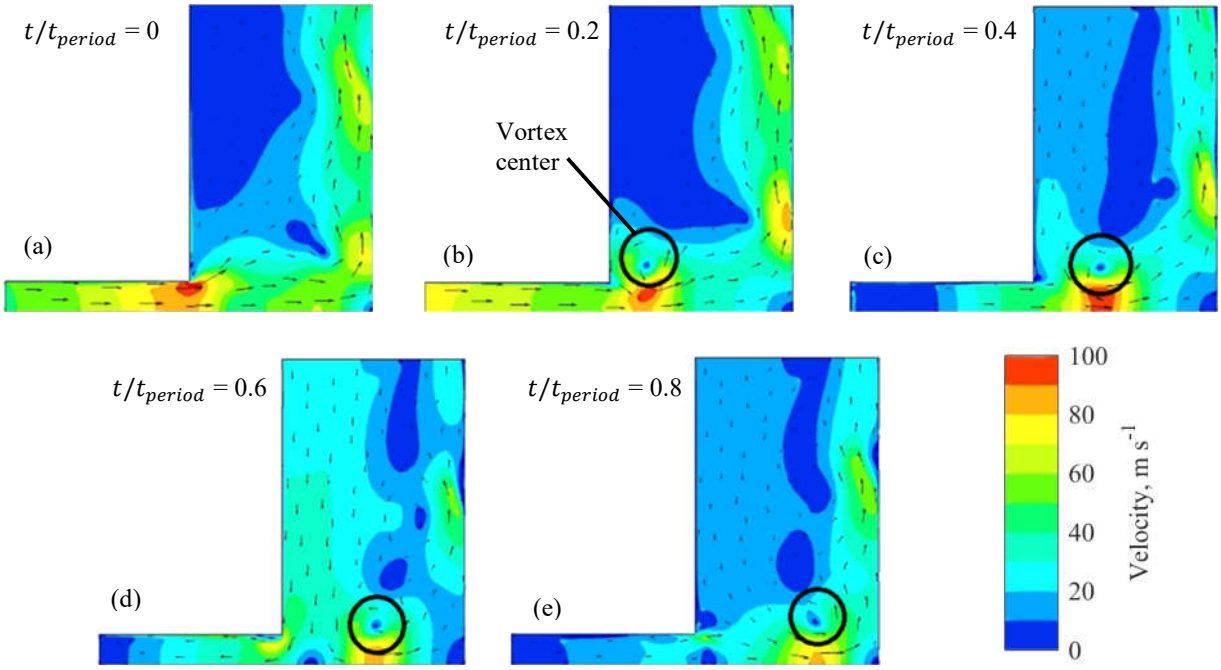

Fig. 11 Velocity magnitude contour plots and vectors for square wave profile (10 kHz, Re = 7074).

IV.Optimization of the fluidic oscillator

In the context of Fig. 11, we demonstrated that there was an optimum *fL/v* (0.08) for Nu enhancement. Such high *fL/v* may be difficult to achieve in practice however because the highest oscillation frequency achieved by the fluidic oscillator in simulations is 1400 Hz (*fL/v* of 0.014) operating at an inlet to outlet pressure ratio of 2.2. Optimization work was conducted to increase *fL/v* for the self-excited fluidic oscillators.

Simplified model to investigate impact of oscillation chamber inlet shape on switching time

To understand the impact of oscillation chamber inlet shape on the switching time, a simplified model was constructed in which the feedback tubes were removed, allowing a switching pressure pulse to be applied directly to the truncated tube inlet. The aim was to modify the shape of the oscillation chamber to reduce the switching time of the oscillator. The simplified geometry is shown in Figure 12.

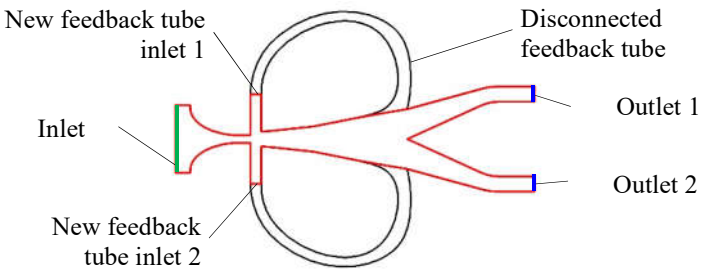

Figure 12: Isolated fluidic oscillator chamber (red) with disconnected feedback tubes (black).

In all cases the outlet pressure was set to $p_2 = 1.01$ bar, and the system pressure ratio to $p_{01}/p_2 = 1.40$. Simulations were initially converged with +0.01 bar (increase from 1.01 bar to 1.02 bar) at the inlet to disconnected feedback tube 2, so that the flow remain attached to the outlet 1 side of the regulator. Once flow was stable, the pressure through feedback tube 2 was reduced to 1.01 bar and simulations were run until the mass flow rate through outlet 1 and outlet 2 stabilized. The flow was in all cases still attached to the outlet 1 side of the regulator (two stable states), but the overall mass flow was reduced slightly because the contribution from the disconnected feedback tube was removed. Once the mass flow rate through both outlets was stable, the solution was saved. The solution was then perturbed by changing the disconnected feedback tube 1 pressure with a step increment equal to between 0.01 and 0.1 bar. For all simulations disconnected feedback tube 2 was set at 1.01 bar. The temporal mass flow rate variation at outlet 1 was recorded after the step in pressure was applied. A sudden drop in outlet mass flow rate corresponds to switching of the stream.

Results are shown in Fig. 13. For pressure steps below 0.0235 bar, the flow fails to switch. For pressure steps greater than 0.0240 bar a rapid switch occurs. Increasing the magnitude of the pressure step increases the speed of the switch and reduces the delay time from the initiation of the pressure pulse. The switch time was defined as the time required for the mass flow rate at outlet 1 to reach 90% of the mass flow change between the initial and final value. The datum was the initiation of the pressure pulse at the inlet to the disconnected tube.

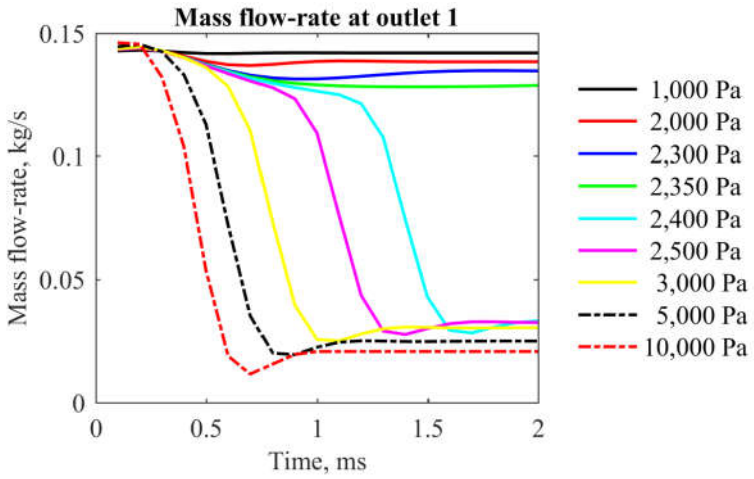

Fig. 13 Mass flow-rate through outlet 1 when a pressure increment is applied to feedback tube 1.

Geometry modifications were then carried out on the shape of the oscillator with the aim of increasing the frequency of oscillating, as represented by faster response times. An alternate aim, beyond the scope of this paper, would be optimisation for minimum threshold switching pressure. This would ensure that the oscillator could still operate at lower inlet to outlet pressure ratios. Classes of shape modification are summarised in Fig. 14. Results for those shape modification, presented as switch time as a function of pressure step size, are shown in Fig. 15.

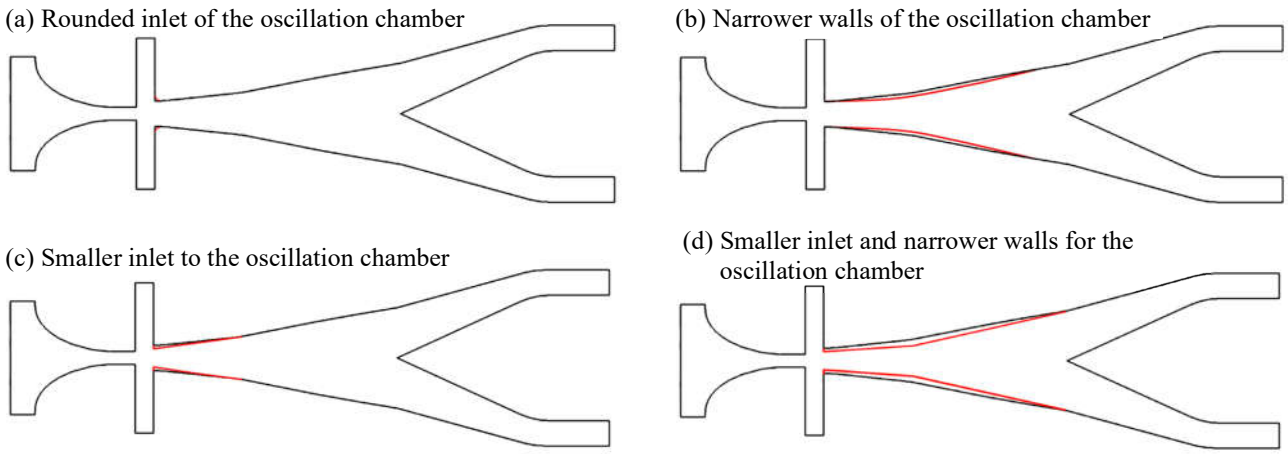

Fig. 14 Modifications done to the fluidic oscillator without feedback tubes.

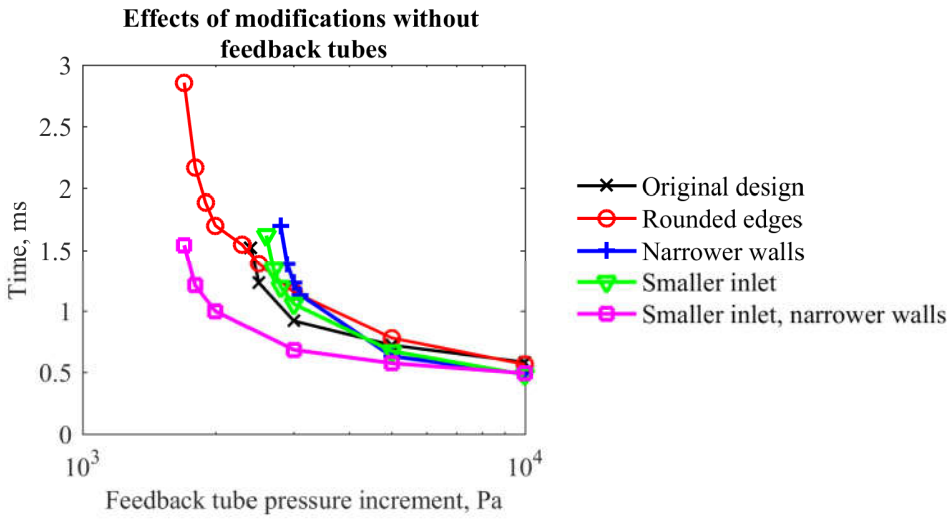

Fig. 15 Response times for modified designs of the fluidic oscillator (disconnected feedback tube model).

Adding rounded edges at the entrance to the oscillation chamber (a) lowered the threshold pressure for switching from approximately 0.0240 bar to approximately 0.0170 bar. The rounded edges encouraged flow from the feedback tube to attach to the downstream side of the main-flow passage (the oscillation chamber). At higher pressures (0.05-0.10 bar), however, the original design achieves a faster response time.

Narrowing the walls of the oscillation chamber (b) improved the response time for high switching pressure step magnitudes (0.05 bar and higher) but worsened the switching time for lower pressures. This modification also increased the minimum switch pressure to approximately 0.028 bar.

Reducing the size of the oscillation chamber inlet (c) slightly improved the response time for high switching pressure step magnitudes (0.05 bar and higher) but at lower feedback pressures, the response time was worsened and the threshold feedback pressure for switching was increased.

Reducing the oscillation chamber inlet size and narrowing the walls of the inlet section to the oscillation chamber (d) both reduced the switching time (by approximately 30%) and also lowered the switching threshold (by approximately 30% from 0.017 bar from 0.024 bar). A summary of results for modifications (a) to (d) in Fig. 14 is show in Table 5.

Table 5 Summary of simulation results for the reduced model of the fluidic oscillator (feedback tubes disconnected).

Design	Threshold pressure to switch, bar	Δt for Δp = 0.05 bar, ms	Δt for Δp = 0.10 bar, ms
Original	0.024	0.722	0.5825
(a)	0.017	0.781	0.5652
(b)	0.028	0.632	0.4869
(c)	0.026	0.674	0.4819
(d)	0.017	0.575	0.4935

Performance investigation of optimized fluidic oscillator

Reducing the oscillation chamber inlet size and narrowing the walls of the inlet section to the oscillation chamber (d) was found to enhance the frequency of oscillation in the reduced model (disconnected feedback tubes). Performance parameters for this geometry in the full environment (feedback tubes reinstated) are now considered.

Fig. 16(a) shows the previous modification (in red) seen in Fig. 14 (d). Two further modifications are show in Fig. 16(b) (modified splitter) and Fig. 16(c) (larger feedback tubes). These further modifications are discussed in this section.

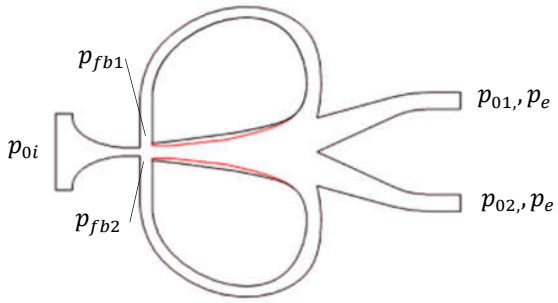

(a) Reduced inlet size and narrower walls

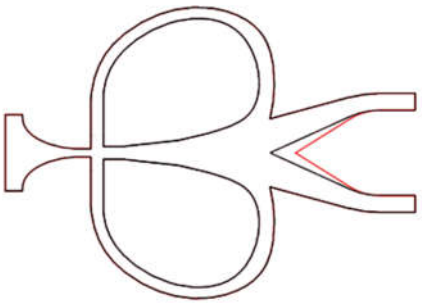

(b) Modified splitter

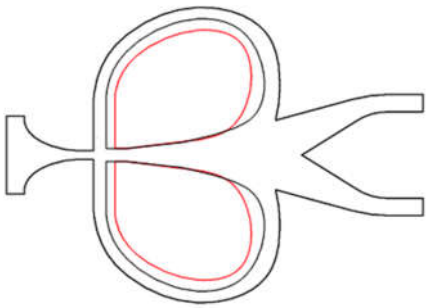

(c) Larger feedback tubes

Fig. 16 Modifications done to the fluidic oscillator with feedback tubes.

To consider the performance of models (a), (b) and (c) in Fig. 16 we define a total pressure loss coefficient

$$\eta = \frac{p_{0i} - \bar{p}_{0e}}{p_{0i} - p_e} \tag{4}$$

where p_{0i} is the inlet total pressure, $\bar{p}_{0e}$ is the time averaged sum of total pressure at the outlets, and p_e is the static pressure at the outlet. The total pressures of the feedback tube flows are evaluated one diameter downstream of the nozzle exit centerlines. The maximum total pressure difference between the feedback tubes injection points (at any point in the cycle) was also calculated, to determine how close the system was to the minimum switching pressure. Results are summarized in Table 6, below.

Table 6 Performance metrics for optimized fluidic oscillator.

Added feature	$\dot{m}$, kg/s	η	$p_{fb1} - p_{fb2}$, Pa	*f*, Hz	fL/v
Original	0.135	0.81	0.0537	769	0.014
Design (d) Fig. 14	0.136	0.82	0.0424	800	0.014
Modified splitter (b) Fig. 16	0.137	0.84	0.0562	952	0.016
Larger feedback tube (c) Fig. 16	0.138	0.82	0.0574	1000	0.017

The optimizations shown in Fig. 16 resulted in increased oscillation frequency by 30%. The highest *fL*/*v* achieved at a pressure ratio of 1.4 was 0.017. This gives rise to a Nu enhancement of 19.5 %, an increase from 15.5 % in the Original case. The frequency of oscillation was found to be very sensitive to the design of the oscillation chamber, and further frequency increases may be possible with a full optimization study, or by increasing jet velocity at high pressure ratios with optimized nozzles shapes.

V.Experiments

An experimental fluidic oscillator was manufactured using the rapid prototyping (SLA) inside a circular housing. This is shown in Fig. 17. The system inlet was 1 mm wide and the system outlets 2 mm wide. A control model with two constant mass flow rate impinging jets was also manufactured (Fig. 17). The control model was used to benchmark the fluidic oscillator in terms

of heat transfer performance at the same mass flow rate. The passage width into the page was 10 mm. A photograph of the internal cavity is shown in Fig. 18.

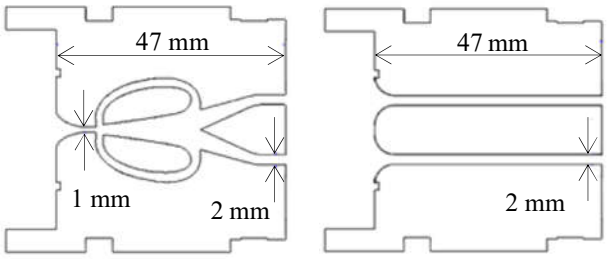

Fig. 17 (L) Drawing of fluidic oscillator for experiment; (R) control system.

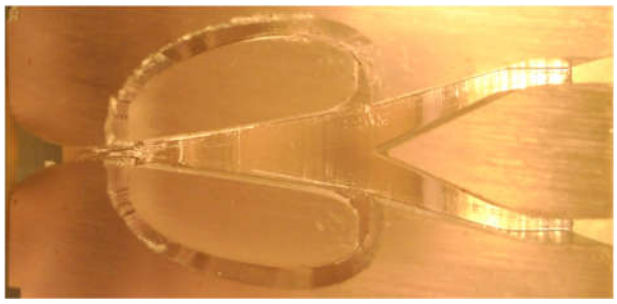

Fig. 18 Internal cavity of the experimental oscillator.

The experimental oscillators were sealed in an aluminum pressure housing as shown in Fig. 19. A calibrated needle valve was used to establish a fixed mass flow rate boundary condition, with a three way ball valve to provide a rapid step in inlet mass flow rate to the oscillator. The flow was arranged to impinge onto interchangeable target surfaces which were instrumented for steady state (calorimeter) or transient (thin film heat flux gauges) experiments. The temperature of the target surface could be increased with a silicone heater pad attached to the rear. A typical pre-heat range was 35–45 °C. Thermocouples were used to measure the flow inlet temperature and the temperature of the target plate.

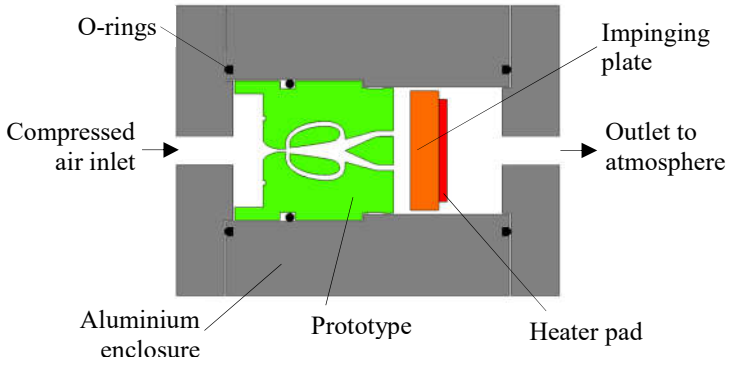

Fig. 19 Cross section schematic of aluminum enclosure and prototype test-piece.

To calibrate the mass flow rate through the needle valve, a cylinder of known volume was filled in a transient experiment. The needle valve was connected to a 6.89 bar line and the flow from the needle valve was vented into the cylinder (volume approximately 0.0139 m^3). A thermocouple was used to measure the internal temperature of the cylinder and to measure the gas temperature.

The mass flow-rate into the cylinder was calculated using the equation

$$\dot{m} = \frac{V}{R}\left(\frac{1}{T}\frac{\dot{dp}}{dt} - \frac{p}{T^2}\frac{dT}{dt}\right) \tag{5}$$

where V is the volume of the cylinder, R is the universal gas constant and T the enclosed gas temperature. The change in temperature with respect to time, dT/dt, was hard to accurately measure due to relatively low flow speeds within the cylinder. For cylinder pressures below 3 bar, very linear trends of pressure against time were observed—as shown in Fig. 20—however, suggesting that compression heating was significantly offset by heat transfer within the cylinder. Experiments for the fluidic oscillator and control case were performed back-to-back, giving low enough error in mass flow rate for the present purpose.

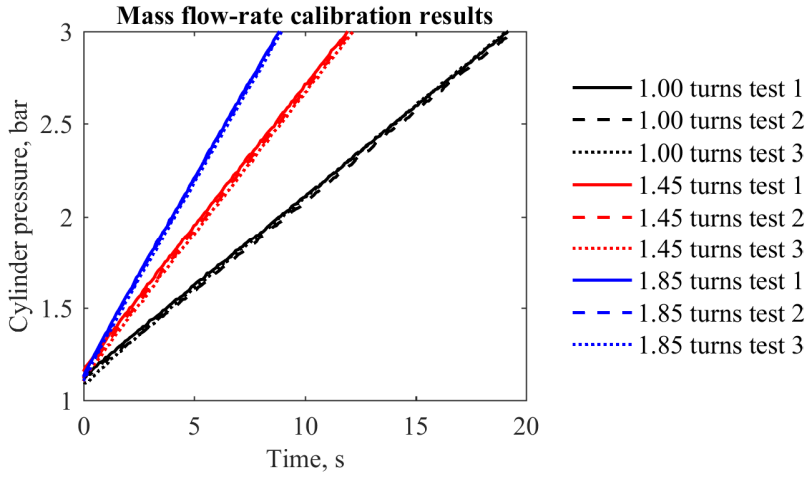

Fig. 20 Typical needle valve calibration results.

Calorimeter experiment

A calorimeter experiment was carried out to determine the area weighted average heat transfer coefficient on the impingement plate. For the calorimeter experiment, a copper target plate (42 mm diameter, 4.8 mm thick) was used (high thermal diffusivity). The low Bi of the experiment (0.005-0.008) allows an isothermal approximation to be used, the plate temperature is measured

with grounded K-type thermocouples. A silicone heater pad was used to set the initial temperature in the range 35–45 °C. The heater pad was off during the cooling phase of the experiment.

The heat flow equation

$$\dot{q} = mc_p \frac{dT_w}{dt} = hA\left(T_w - T_g\right) \tag{6}$$

can be solved under quasi-steady conditions (calorimeter equation) to give a normalized temperature

$$\theta = \frac{T_w - T_g}{T_{wi} - T_{gi}} = exp\left(\frac{-t}{\tau}\right) \tag{7}$$

where $\tau = \mathrm{mc_p}/hA$ is the time constant of temperature decay, m is the mass of the target plate (calorimeter), c_p is the specific heat capacity of the target plate (copper), h is the are-averaged heat transfer coefficient, A is the surface area of the target plate T_w is the temperature of the copper plate, T_g is the gas inlet temperature, and the subscript i denotes the initial temperatures. A value of τ is found iteratively, allowing h and Nu to be evaluated. Uncertainty calculations are presented in Table 7. The estimated absolute uncertainty in Nu (95% confidence) was 5.6 %.

Table 7 Uncertainty analysis for calorimeter data.

Parameters	Nominal range/value	Maximum uncertainty, %
Target plate temperature, T_w	290 – 315 K	0.75
Gas inlet temperature, T_g	~290 K	0.75
Time constant of temperature decay, τ	24 – 42 s	1.2
Thickness of target plate	4.8 mm	2.1
Heat transfer coefficient, h	392-655 W m^{-2} K	2.4
Outlet width, L	2 mm	5.0
Nusselt number, Nu	30 – 50	5.6

Normalized experimental temperature against time plots for the calorimeter experiments are shown in Fig. 21 along with the best fit of Equation 7 to the data. The jet Reynolds number was based on a characteristic length L equal to the outlet passage width (2 mm) and the average velocity of the flow through one outlet. The excellent agreement of the form of Equation 7 to the data should be noted.

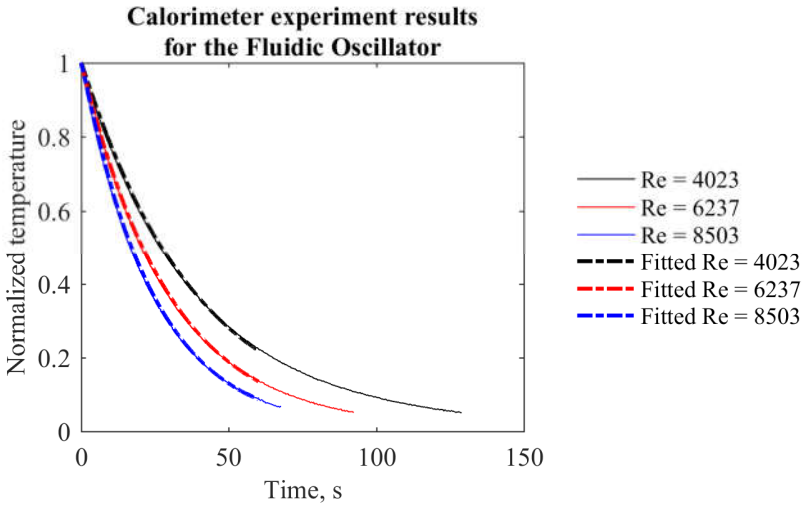

Fig. 21 Typical experimental results for the calorimeter experiment.

A summary of the experimental results for calorimeter experiments for both the fluidic oscillator and the control case are shown in Fig. 22. Here surface averaged Nu (outlet width, L = 2 mm) is plotted against jet Re (characteristic length L equal to one outlet width of 2 mm and velocity equal to average velocity of the flow through one outlet). 2D simulation results are also presented by taking the average Nu from results in Fig. 8. At zero mass flow-rate, the modest heat transfer coefficient represents the heat loss rate due to conduction. The 2D simulation results have been adjusted by adding the zero mass flow conduction offset.

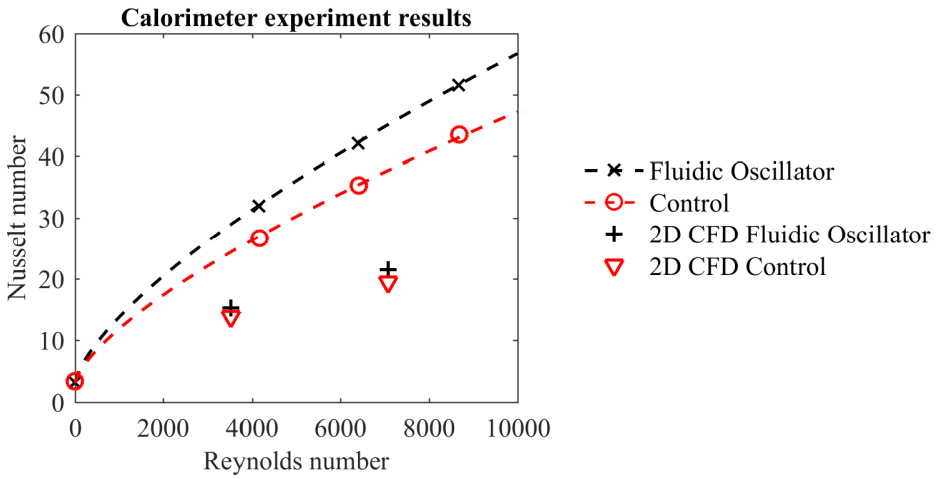

Fig. 22 Summary experimental results for calorimeter experiment: surface averaged Nu as a function of jet Re.

All results for the oscillator were at least 20% higher than the control case, demonstrating the expected enhancement in heat transfer coefficient. The data are well behaved, showing approximately constant enhancement across the range tested. Experimental results are well fitted by a correlation of the form $\mathrm{Nu} = c\mathrm{Re}^{a}$, where a = 0.7 and c is a constant. This is in closer agreement with [4] than flat plate correlations (a = 0.5). It should be noted that the 2D CFD results are from only one jet impinging onto the plate while the experiments results are of two jets impinging onto the plate. Thus, poor absolute agreement with the 2D CFD results is expected. The purpose of the comparison is to look at the enhancement due to oscillation in both the experimental and numerical results. The *fL/v* value for the fluidic oscillator experimentally tested was approximately 0.009. 2D heat transfer simulations (Fig. 10) predicted an enhancement of 45% over the constant mass flow case. However, only 20% enhancement was observed in the calorimeter experiment. This is discussed further in the context of the heat transfer coefficient distributions measured in the transient experiments.

Transient experiments

Surface heat transfer measurements were conducted using thin-film platinum resistance heat transfer gauges of the type described by [31]. A thin polyimide substrate was used to support the gauges and was mounted to 10 mm thick aluminum target plate using a thin glue layer (3M VHB 9460) of a type described in [32]. Two thermocouples were located as near as possible to the metal surface. A photograph of the gauges and a diagram of the gauge construction is shown in Fig. 23. Seven gauges were used in this test, distributed along a line crossing a diameter of the target plate. A silicone heater pad was used to set the initial temperature in the range 35–45 °C. The heater pad was off during the cooling phase of the experiment.

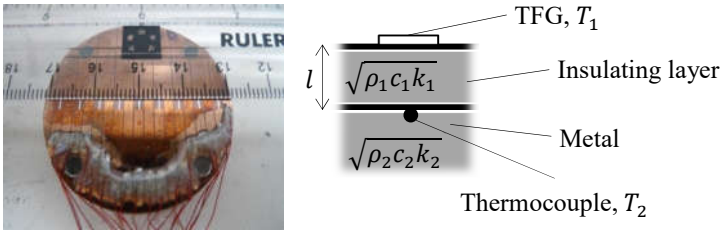

Fig. 23 (L) Photograph of the thin film gauges; (R) diagram of gauge construction adapted from [32]**.**

The thin film gauges (TFGs) were operated in a constant-current mode. In this mode, the gauge voltage drop is proportional to the sensor resistance, which depends on temperature. The surface temperature, T_1 is related to the gauge resistance by equation

$$R = R_0 + \alpha T_1 \tag{8}$$

where R_0 is the resistance at 0 ºC and α is the temperature coefficient of resistance. The value of α was obtained from calibration in a water bath. The voltage signals from the thin film gauges were passed through an amplifier and the voltage was measured using a National Instruments NI 9205 card sampling at 5 kHz. The measured voltage was converted to temperature using the equation

$$T_1 - T_{2i} = \frac{(V - V_i)R_i}{\alpha G V_{HTA}} \tag{9}$$

where T_{2i} is the initial temperature measured using the K-type thermocouple, V_i is the average voltage before the step recorded using the NI 9205 card, R_i is the resistance at T_{2i} which was calculated using the resistance equation 8, G is the amplifier gain and V_{HTA} is the voltage set in the HTA which provides the TFGs with the constant current.

The local heat flux on the surface of the impingement plate was calculated as follows

$$\dot{q} = k\frac{T_2 - T_1}{l} \tag{10}$$

Thus, the heat transfer coefficient was given by

$$h = \frac{q}{T_1 - T_g} \tag{11}$$

where T_g is the inlet gas temperature. The uncertainties in individual measurements are presented in Table 8. The estimated absolute uncertainty in Nu (95% confidence) was 13.7 %.

Table 8 Uncertainty analysis for TFG data.

Parameters	Nominal value	Maximum uncertainty, %
Temperature coefficient of resistance, α	0.038 Ω K^{-1}	0.8
Initial resistance, R_i	27.3 Ω	0.6
Initial gauge voltage, V_{HTA}	0.25 V	2.0
Voltage difference, V - V_i	0.05 V	0.3
Amplifier gain, G	50	6.0
Initial temperature, T_0	303 K	0.5
Gauge temperature, T_g	(varies)	6.9
Aluminum temperature, T_2	303 K	0.5
Kapton-plus-glue thickness, l	100 μm	5.0
Heat flux, $\dot{q}$	(varies)	8.9
Heat transfer coefficient, h	190 – 830 W m^{-2} K	11.5
Nusselt number, Nu	14 – 64	13.7

Fig. 24 shows the typical temperature response of the TFGs to flow. In this example the sample piece was supplied with a mass flow-rate of 1.58 g/s (Re = 4023). Flow is initiated at approximately 1.5 s causing a sudden drop in surface temperature (1.5 – 1.8 s, the unsteady response of surface) followed by a quasi-steady decay in surface temperature (1.8 – 10 s, gauge now in *steady-state* mode, and the target plate acting as a calorimeter).

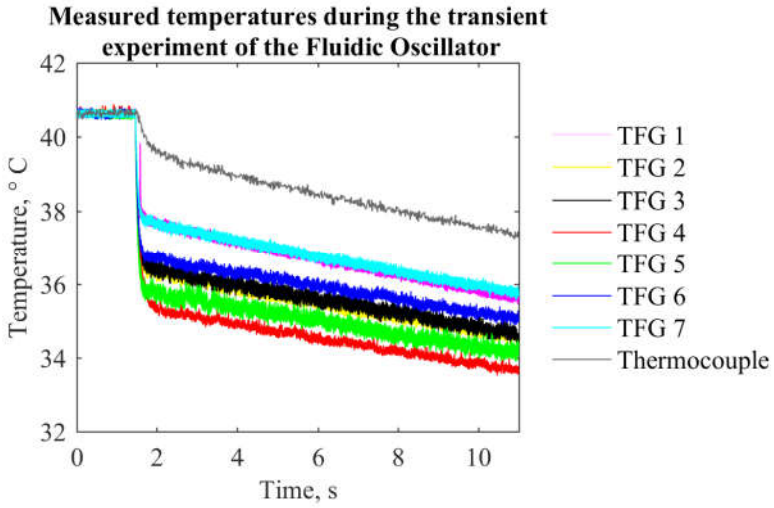

Fig. 24 TFG temperature responses to a sudden step in flow.

The temperature data in Fig. 24 (period 3 s to 8 s, TFG5 located under an impinging jet) were used to compute power spectrums for the fluidic oscillator and control at different Re conditions shown in Fig. 25. Results for the fluidic oscillator show a very clear peaks in power, marking the frequency of oscillation. The peak reduces in strength and shifts higher in frequency as Re is increased. The control experiments show broad band frequency content associated with unsteadiness, but with no well-defined peaks.

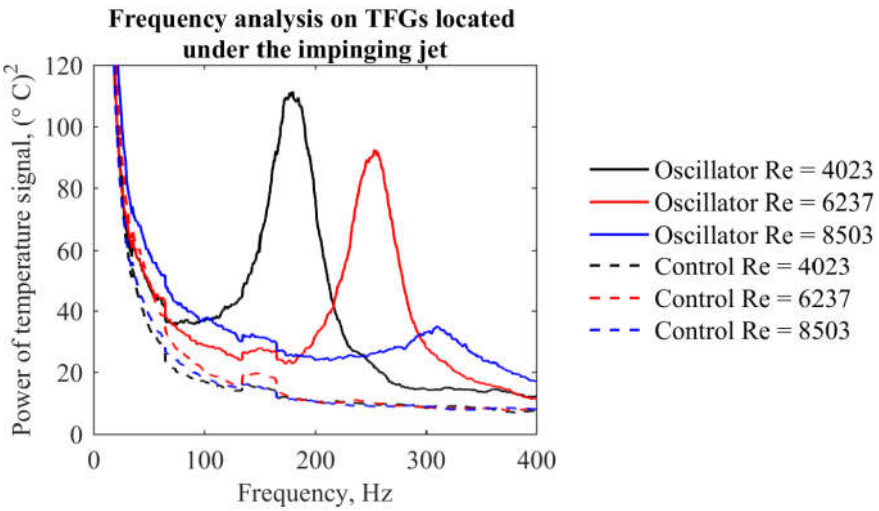

Fig. 25 Power spectrums obtained from measurements of surface temperature.

Fig. 26 shows the oscillation frequency as a function of jet Re for three experiments using the same test piece. Also shown are the CFD predictions which are halved from Fig. 4 because the device length scale (nozzle throat to splitter distance) in the experiments is twice that of the CFD simulations. This is done in accordance to the results of the length scale effects study in Table 1. The experiment data are in reasonable agreement with the linear trend predicted with CFD. The oscillation frequencies measured experimentally were approximately 30% lower than those predicted previously. The difference is thought to be due to inaccurate forming of the oscillation chamber in the manufacturing process (ratio to internal jet width too high). To calculate the heat transfer coefficient, the method described by [32] was used. The temperatures at the top and bottom surfaces of the layer are measured using the TFG and thermocouple respectively. The surface temperature of a two-layer substrate (polyamide/glue and aluminum) is initially dominated by the thermal product of the polyamide/glue layer, $\rho_1 c_1 k_1$ [33]. Once the thermal wave has penetrated the polyamide/glue layer, the gauge acts like a direct heat-flux gauge [34]. In this period the surface temperature rises much more slowly and is now most strongly linked to $\rho_2 c_2 k_2$, the thermal product of the aluminum layer. In the present situation in the second period the system acts like an insulated (additional thermal resistance) calorimeter. The polyamide/glue layer is treated as one homogeneous layer because the thermal properties are similar.

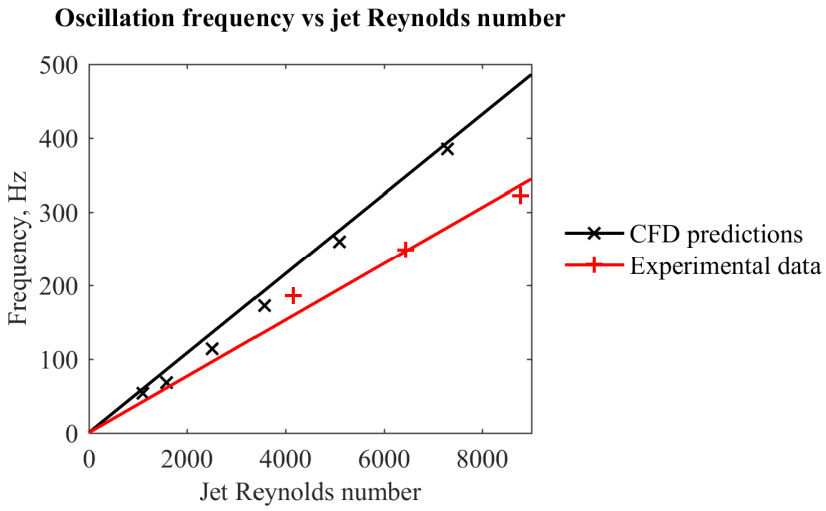

Fig. 26 Oscillation frequency as a function of jet Re.

Fig. 27 shows the temperature of the TFG against the square root of time for the transient experiment. It can be seen after approximately 0.4 $s^{1/2}$ (0.16 s), the temperature decays much more slowly and the TFG acts as a direct heat-flux gauge.

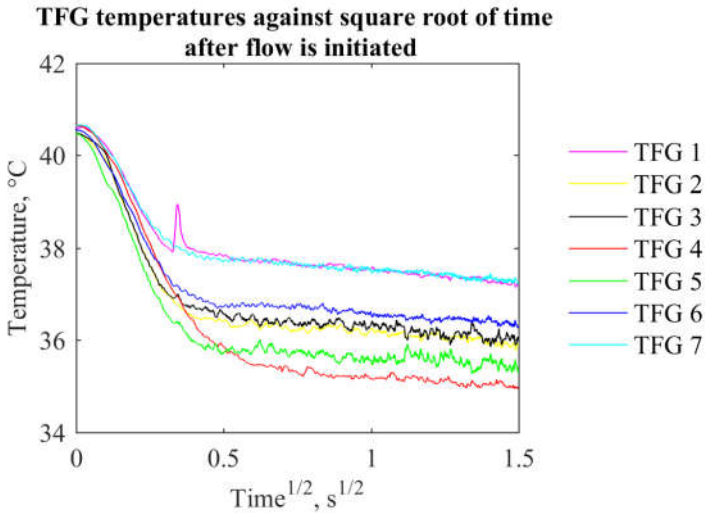

Fig. 27 Typical transient temperature response of TFGs exposed to a temperature step.

Fig. 28 shows the heat flux measured during a typical experiment. Flow is initiated at approximately 1.5 s. At approximately 2 s, the gauge is operating in steady state mode. Average values of *h* were obtained over a period of 1 s (marked with grey band), and turned into Nu values using a reference length equal to the nozzle width (2 mm).

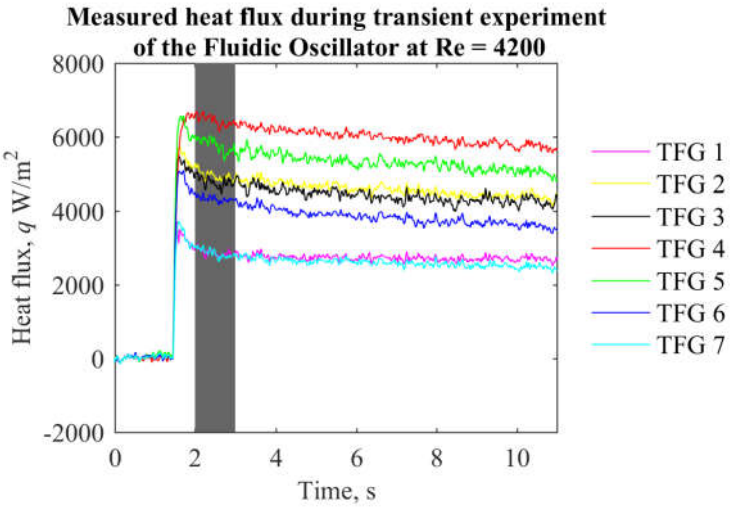

Fig. 28 Local heat flux measured during a typical transient experiment.

Summary results of the transient experiment are shown in Fig. 29. Results for both the fluidic oscillator and the control test piece are shown at a variety of Re. The estimated error in the alignment of the target plate, and therefore the location of the impinging jets, was ±1 mm. The fluidic oscillator showed significantly improved Nu over the control case in between the two impinging jets. The data are too sparse to obtain a meaningful area average, but the improvement is consistent with the 20% improvement measured in calorimeter tests.

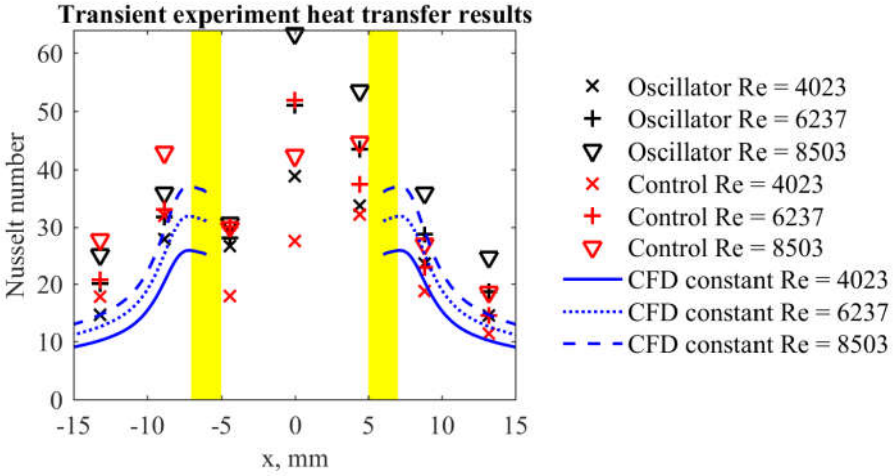

Fig. 29 Summary of Nu values on the target plate.

VI. Conclusions

A fluidic oscillator was designed and optimized based on 2D computational fluid dynamic simulations. The direct proportional behavior of the frequency versus the volumetric flow-rate agrees with previous experimental results in the literature. A higher volumetric flow-rate corresponds to a higher nozzle jet velocity and also a higher velocity in the feedback tubes. The switching time is thought to be dominated by through-flow time rather than pure acoustic (speed of sound) effects. The effect of Re on f is greater at lower pressure ratios, resulting in an increase in f of up to 221 % in the range $1.01 < p_{01}/p_2 < 1.10$.

Heat transfer simulations showed that Nu enhancement due to oscillatory flow increased up to $fL/v = 0.08$, followed by a steep trough, with a second increase in the enhancement for $fL/v > 0.50$. The frequency dependent enhancement over the steady state case was as much as 240% for high fL/v values. The peak in Nu enhancement was associated with a jet-excited vortex formation, pumped by the oscillating jet. This is postulated as the possible cause of significantly enhanced predicted heat transfer rates. For realistically achievable values of fL/v, Nu enhancement of approximately 45% was predicted.

Experiments on a fluidic oscillator showed a very clear peak in the power spectrum which reduced in strength and shifted higher in frequency as Re was increased, in line with computational predictions. The oscillation frequencies measured experimentally were approximately 30% lower than those predicted computationally. The difference was thought to be due to inaccurate forming of the oscillation chamber in the manufacturing process, rather than demonstrating a weakness in the CFD.

Experimental results shows 20% enhancement of Nu over the control case in a calorimeter test with a circular target plate. This result was consistent over a wide range of Re conditions. Local measurements with thin film heat transfer gauges demonstrated that the enhancement in Nu was largely the result of enhancement *between* the impinging jets. Nu measurements for the oscillating and non-oscillating flows were similar outside this region. The fL/v value for fluidic oscillator tested was approximately 0.009, and 2D heat transfer simulations predicted an enhancement of 45% over the constant mass flow case. The two results are broadly consistent, when the difference between the 3D and 2D environments are considered. Results from tests on fluidic oscillator arrays would be required to establish correct surface average values in most practical situations.

There are applications in which fluidic oscillators may have practical application in delivering periodic coolant flow in moving systems. Examples include delivering flow to a rotor disc, the tip of a rotor blade, to a moving seal cavity etc. Gas turbines typically have a disk passing frequency around 100-200 Hz, and a blade passing frequency of typically 6,000-10,000 Hz. In principle, higher oscillation frequencies could be achieved by implementing an externally-energized motive flow (piezo-actuated valve, spinning valve, spark energized pulse, resonant tube etc.), rather than using a self-excited system. In very high frequency systems (6,000–10,000 Hz) such as those describe above, at useful scales found practical by engineers for coolant

delivery (holes >0.5 mm diameter, and several mm long) transit times become limited by the acoustic wave speed. In the view of the authors, switching devices of the type discussed here are unlikely to be implemented successfully due to fundamental scaling issues (wave speed versus hole length) at practical size. One must also consider that gains due to periodic fluid delivery (targeted at rotor tip, or a rotor shank cavity, for example, at a particular point in the cycle) would in most systems be more than offset by the large attendant pressure losses in fluidic devices of the type described. It seems unlikely that a fluidic oscillator would find a home in the control of such systems.

There is a limited class of problem where pure acoustic effects, self-excited by an external pressure wave of high frequency and magnitude, can provide a similar result to the fluidic switching mechanism described in this paper, but with low loss and practically implementable in the 6,000–10,000 Hz frequency range. A system which capitalized on the pure acoustic wave effect, successfully implemented in gas turbine test vehicles, is described by [12]. The operating mechanism (the *physics*) of the acoustically tuned hole is very different to the fluidic oscillator described here.

In systems where the periodic flow is purely a means of achieving enhanced heat transfer, although the practically achievable 40% increase in Nu, and the theoretically achievable 240% Nu enhancement, are tempting to the designer, it is hard to imagine the class of system which would benefit from the fluidic oscillators considered in this research. This is because extreme pressure losses are incurred in the oscillation chamber, reducing the potential to promote heat transfer by more conventional means. The theoretical system which would benefit from the fluidic oscillator purely as a means to enhance heat transfer is one in which the coolant mass flow is fixed, the jet velocity to the target plate has a fixed upper limit (momentum considerations, perhaps), and in which pumping work is not counted in the overall system optimization. This represents a rather unusual set of optimization goals.

We conclude that the self-excited oscillator, whilst interesting in the abstract, may struggle to find a heat transfer problem for which it is a natural solution when whole-system optimization is considered. We also hope to be proved wrong.

References

[1] R. Gardon and J. C. Akfirat, “The role of turbulence in determining the heat-transfer characteristics of impinging jets,” *International Journal of Heat and Mass Transfer*, Vol. 8, No. 10, 1965, pp. 1261–1272. doi: 10.1016/0017-9310(65)90054-2

[2] C. J. Hoogendoorn, “The effect of turbulence on heat transfer at a stagnation point,” *International Journal of Heat and Mass Transfer*, Vol. 20, No. 12, 1977, pp. 1333–1338.

doi: 10.1016/0017-9310(77)90029-1

[3] H. Martin, “Heat and Mass Transfer between Impinging Gas Jets and Solid Surfaces,” *Advances in Heat Transfer*, Vol. 13, 1977, pp. 1–60.
doi: 10.1016/S0065-2717(08)70221-1

[4] K. Jambunathan, E. Lai, M. A. Moss, and B. L. Button, “A review of heat transfer data for single circular jet impingement,” *International Journal of Heat and Fluid Flow*, Vol. 13, No. 2, 1992, pp. 106–115.
doi: 10.1016/0142-727X(92)90017-4

[5] R. Viskanta, “Heat transfer to impinging isothermal gas and flame jets,” *Experimental Thermal and Fluid Science.*, Vol. 6, No. 2, 1993, pp. 111–134.
doi: 10.1016/0894-1777(93)90022-B

[6] B. N. Hewakandamby, “A numerical study of heat transfer performance of oscillatory impinging jets,” *International Journal of Heat and Mass Transfer*, Vol. 52, No. 1, 2009, pp. 396–406.
doi: 10.1016/j.ijheatmasstransfer.2008.07.004

[7] P. Xu, B. Yu, S. Qiu, H. J. Poh, and A. S. Mujumdar, “Turbulent impinging jet heat transfer enhancement due to intermittent pulsation,” *International Journal of Thermal Sciences*, Vol. 49, No. 7, 2010, pp. 1247–1252.
doi: 10.1016/j.ijthermalsci.2010.01.020

[8] H. S. Sheriff and D. A. Zumbrunnen, “Effect of Flow Pulsations on the Cooling Effectiveness of an Impinging Jet,” *Journal of Heat Transfer*, Vol. 116, No. 4, 1994 , p. 886.
doi: 10.1115/1.2911463

[9] R. C. Behera, P. Dutta, and K. Srinivasan, “Numerical Study of Interrupted Impinging Jets for Cooling of Electronics,” *IEEE Transactions on Components and Packaging Technologies*, Vol. 30, No. 2, 2007, pp. 275–284.
doi: 10.1109/TCAPT.2007.898353

[10] H. M. Hofmann, D. L. Movileanu, M. Kind, and H. Martin, “Influence of a pulsation on heat transfer and flow structure in submerged impinging jets,” *International Journal of Heat and Mass Transfer*, Vol. 50, No. 17, 2007, pp. 3638–3648.
doi: 10.1109/TCAPT.2007.898353

[11] E. C. Mladin and D. A. Zumbrunnen, “Local convective heat transfer to submerged pulsating jets,” *International Journal of Heat and Mass Transfer*, Vol. 40, No. 14, 1997, pp. 3305–3321.

doi: 10.1016/S0017-9310(96)00380-8

[12] M. Collins and T. Povey, "Exploitation of Acoustic Effects in Film Cooling," *Journal of Engineering for Gas Turbines and Power*, Vol. 137, No. 10, 2015, p. 102602.
doi: 10.1115/1.4030102

[13] C. Gau, W. Y. Sheu, and C. H. Shen, "Impingement Cooling Flow and Heat Transfer Under Acoustic Excitations," *Journal of Heat Transfer*, Vol. 119, No. 4, 1997, p. 810.
doi: 10.1115/1.2824187

[14] C. Camci and F. Herr, "Forced Convection Heat Transfer Enhancement Using a Self-Oscillating Impinging Planar Jet," *Journal of Heat Transfer*, Vol. 124, 2002, p. 770.
doi: 10.1115/1.1471521

[15] L. Agricola, M. A. Hossain, R. Prenter and R. Lundgreen, "Impinging Sweeping Jet Heat Transfer," *Proceedings of the Fifty Third AIAA/SAE/ASEE Joint Propulsion Conference*, AIAA, Atlanta, GA, 2017, p. 4974.
doi: 10.2514/6.2017-4974

[16] T. Koso, T. Saito, and K. Tsukahara, "Numerical Simulation on Self-Induced Oscillation of a Low Reynolds Number Jet in Fluidic Oscillators.," *Proceedings of the Japan Society of Mechanical Engineers Kyushu Branch*, Vol. 2007, No. 60, 2007, pp. 161–162.

[17] V. Tesař, "Fluidic control of reactor flow—Pressure drop matching," *Chemical Engineering Research and Design*, Vol. 87, No. 6, 2009, pp. 817–832.
doi: 10.1016/j.cherd.2008.11.004

[18] B. E. Launder and D. B. Spalding, *Lectures in mathematical models of turbulence*. London; New York: Academic Press, 1972.

[19] R. H. Aungier, "A Fast, Accurate Real Gas Equation of State for Fluid Dynamic Analysis Applications," *Journal of Fluids Engineering*, Vol. 117, No. 2, 1995, p. 277.
doi: 10.1115/1.2817141

[20] W. Sutherland, "The viscosity of gases and molecular force," *Philosophical Magazine Series 5*, Vol. 36, No. 223, 1893, pp. 507–531.
doi: 10.1080/14786449308620508

[21] J.-T. Yang, C.-K. Chen, K.-J. Tsai, W.-Z. Lin, and H.-J. Sheen, "A novel fluidic oscillator incorporating step-shaped

attachment walls," *Sensors and Actuators A: Physical*, Vol. 135, No. 2, 2007, pp. 476–483.
doi: 10.1016/j.sna.2006.09.016

[22] M. Behnia, S. Parneix, Y. Shabany, and P. A. Durbin, "Numerical study of turbulent heat transfer in confined and unconfined impinging jets," *International Journal of Heat and Fluid Flow*, Vol. 20, No. 1, 1999, pp. 1–9.
doi: 10.1016/S0142-727X(98)10040-1

[23] J. W. Baughn and S. Shimizu, "Heat Transfer Measurements From a Surface With Uniform Heat Flux and an Impinging Jet," *Journal of Heat Transfer*, Vol. 111, No. 4, 1989, p. 1096.
doi: 10.1115/1.3250776

[24] D. W. Colucci and R. Viskanta, "Effect of nozzle geometry on local convective heat transfer to a confined impinging air jet," *Experimental Thermal and Fluid Science*, Vol. 13, No. 1, 1996, pp. 71–80.
doi: 10.1016/0894-1777(96)00015-5

[25] D. Lytle and B. W. Webb, "Air jet impingement heat transfer at low nozzle-plate spacings," *International Journal of Heat and Mass Transfer*, Vol. 37, No. 12, 1994, pp. 1687–1697.
doi: 10.1016/0017-9310(94)90059-0

[26] F. R. Menter, "Two-equation eddy-viscosity turbulence models for engineering applications," *AIAA Journal*, Vol. 32, No. 8, 1994, pp. 1598–1605.
doi: 10.2514/3.12149

[27] P. Spalart and S. Allmaras, "A one-equation turbulence model for aerodynamic flows," in *30th Aerospace Sciences Meeting and Exhibit*, 1992.
doi: 10.2514/6.1992-439

[28] S. Spring, D. Lauffer, B. Weigand, and M. Hase, "Experimental and Numerical Investigation of Impingement Cooling in a Combustor Liner Heat Shield," *Journal of Turbomachinery*, Vol. 132, No. 1, 2010, p. 11003.
doi: 10.1115/1.3103924

[29] W. M. Kays, M. E. Crawford, and B. Weigand, *Convective heat and mass transfer.* McGraw-Hill Higher Education, 2005.

[30] B. Han, R. J. Goldstein, "Instantaneous energy separation in a free jet. Part I. Flow measurement and visualization," *International Journal of Head and Mass Transfer*, Vol. 46, 2003, pp. 3975-3981
doi: 10.1016/S0017-9310(03)00245-X

[31] J. E. Doorly and M. L. G. Oldfield, “New Heat Transfer Gages for Use on Multilayered Substrates,” *Journal of Turbomachinery*, Vol. 108, No. 1, 1986, p. 153.
doi: 10.1115/1.3262015

[32] E. Piccini, S. M. Guo, and T. V Jones, “The development of a new direct-heat-flux gauge for heat-transfer facilities,” *Measurement Science and Technology*, Vol. 11, No. 4, 2000, pp. 342–349.
doi: 10.1088/0957-0233/11/4/302

[33] T. Povey, K. S. Chana, T. V. Jones, and J. Hurrion, “The Effect of Hot-Streaks on HP Vane Surface and Endwall Heat Transfer: An Experimental and Numerical Study,” *Journal of Turbomachinery*, Vol. 129, No. 1, 2007, p. 32.
doi: 10.1115/1.2370748

[34] A. H. Epstein, G. R. Guenette, R. J. G. Norton, and C. Yuzhang, “High-frequency response heat-flux gauge,” *Review of Scientific Instruments*, Vol. 57, No. 4, 1986, p. 639.
doi: 10.1063/1.1138882